

Porosity in Thick Section Alloy 690 Welds – Experiments, Modeling, Mechanism, and Remedy

Analyzing the characteristics of laser and hybrid laser-gas metal arc welded Alloy 690 with a compositionally identical filler metal

BY J. J. BLECHER, T. A. PALMER, AND T. DEBROY

ABSTRACT

Laser and hybrid laser-arc welding present significant opportunities for thick section welding of nickel-based alloys during the construction and repair of nuclear power plant components. However, the impact of these welding processes on the fusion zone geometry and defect levels in Alloy 690 are not well understood. A series of laser and hybrid laser-gas metal arc welds were fabricated with varying laser powers and welding speeds. The internal macroporosity remaining after welding was characterized using x-ray computed tomography. While the porosity levels attributed to key-hole instability and collapse remained high in the laser welds for all power levels, the addition of the arc in the hybrid laser-arc welds inhibited the formation of porosity at laser powers in excess of 4 kW. A well-tested three-dimensional heat transfer and fluid flow model was used to determine both the geometry of the fusion zone and the region of mixing of the filler metal within the weld pool for various welding variables. By correlating the geometries of the weld pool and the volume of the filler metal mixing region with the experimentally determined porosity, significant insight can be obtained about the mechanism of porosity reduction in hybrid laser-arc welding. At lower laser powers, a combination of high-speed filler metal addition and small pool size prevented the bubbles from escaping. The experimental and calculated results show that porosity in Alloy 690 hybrid welds can be eliminated if the laser heat input and arc conditions are properly selected to avoid the bubble being trapped in the weld pool. The mechanistic understanding uncovered in the work is used to develop a process map showing the important combination of welding variables for producing porosity-free hybrid welds.

KEYWORDS

- Alloy 690 • Ni-Based Alloy • Laser Welding • Hybrid Laser-Arc Welding
- Porosity • X-Ray CT

Introduction

Joining thick sections of Inconel® Alloy 690, a Ni-Cr-Fe alloy, is critical for the construction and repair of nuclear power plants (Ref. 1). The current joining techniques include submerged arc welding (SAW) (Refs. 2, 3) and gas tungsten arc welding (GTAW)

(Refs. 4–6). These traditional welding processes are widely available, but they are limited by slow welding speeds, high heat inputs, and shallow weld penetrations, which require a large number of passes to fabricate thick section components in excess of 6 mm (Ref. 4). Laser and hybrid laser-gas metal arc (GMA) welding processes

produce deeper penetrations per pass and reduce the total heat input compared to arc welding, limiting distortion and heat-affected zone size (Ref. 7). While the advantages of laser and hybrid laser-arc welding show promise for joining Alloy 690, high levels of porosity hinder their wider deployment in power plant component fabrication (Refs. 8–10).

To identify and implement methods to eliminate porosity in Alloy 690 welds, a combined experimental and modeling analysis of the process detailing the complex interactions occurring in the weld must be undertaken. Over a range of laser powers and welding speeds, the effects of laser and hybrid laser-gas metal arc welding processes on weld shape and size and porosity formation have been compared. X-ray computed tomography (CT) has been used to characterize the size and location of pores in the laser and hybrid laser-arc welds.

The filler metal-molten pool mixing region and the heat transfer and fluid flow during welding are modeled to identify the porosity mechanism in hybrid welds and aid the development of remediation strategies. Utilizing an analytical model (Refs. 11–14), the dimensions of the filler metal-molten pool mixing region can be estimated, and its effect on bubble escape analyzed. A well-tested, three-dimensional (3D) heat transfer and fluid flow numerical model (Refs. 12, 15–17) is used to calculate the temperature and fluid velocity fields during laser and hybrid welding. The 3D weld pool

J. J. BLECHER, T. A. PALMER, and T. DEBROY are with the Department of Materials Science and Engineering, The Pennsylvania State University, University Park, Pa. PALMER is also with the Applied Research Laboratory, The Pennsylvania State University, University Park, Pa.

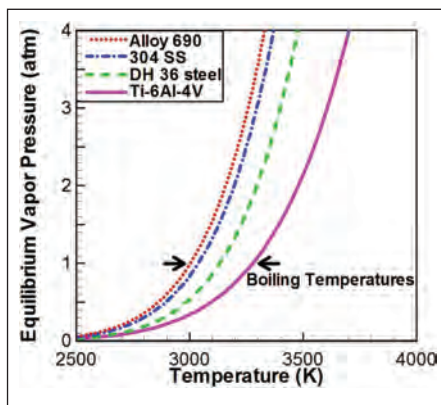


Fig. 1 — The vapor pressure-temperature relations may explain why increased porosity is observed in Alloy 690 welds compared to other common engineering alloys.

geometry is an important factor in bubble entrapment and porosity formation and can be determined using the numerical model.

In general, the keyhole formed during high-intensity beam welding is unstable and the origin for macroporosity observed in laser welds (Ref. 18). The mechanism controlling high porosity in hybrid welds is linked to the consumable filler metal electrode entering the molten weld pool at high speeds greater than 1 m/s. When combined with low laser powers and shallow weld pools, the filler metal addition inhibits the upward motion of bubbles and results in high levels of porosity. At higher laser powers, the pool is deeper and larger, in general, compared to the region where filler metal is entering the pool, so bubbles avoid being trapped in the advancing solid-liquid interface due to the increased pool size and available liquid metal below the filler metal-molten pool mixing region.

The remedy for high porosity requires appropriate selection of welding parameters, including welding speed, laser power, arc current, arc voltage, wire feed speed, and wire electrode diameter. The principle for parameter selection is to increase the opening between the bottom of the mixing region, which depends on arc current, wire feed speed, and electrode diameter, and the bottom of the weld, which is governed by welding speed and laser power. The minimum opening is found to be 3.2 mm, based on the experiments performed here. Based on the

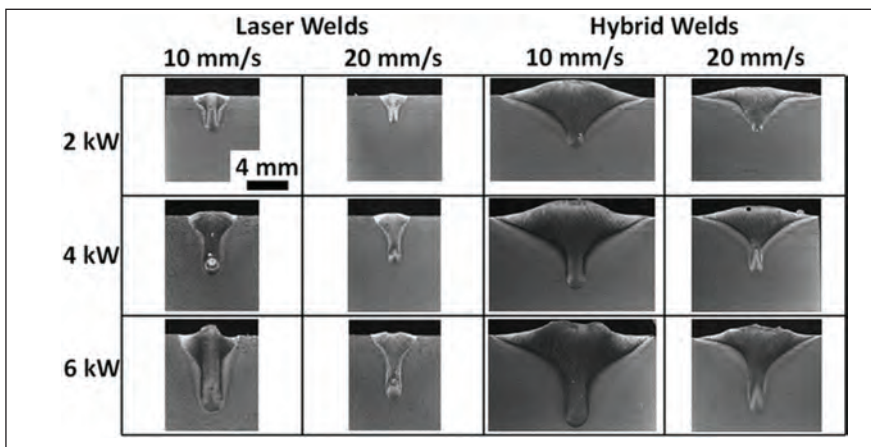


Fig. 2 — Laser and hybrid laser-weld transverse cross-sections of Alloy 690 are shown. The additional heat source in the hybrid welds produces much larger welds with lower aspect ratios.

experiments and modeling of the filler metal-molten pool mixing region, a process map has been constructed, showing the combination of process parameters that will result in low porosity hybrid welds.

Background

Several researchers have investigated the effects of laser welding on Alloy 690 weld geometry (Refs. 8–10, 19–21) and porosity (Refs. 19–21). These previous studies have been limited to laser powers of 5.5 kW or less and resulted in complete joint penetration welds with a maximum depth of 3 mm and partial penetration welds with depths of 6 mm or less. These low-power laser welds in Alloy 690 have a high depth-to-width ratio (Refs. 8–10, 19–21) similar to that observed in laser welding other common structural alloys (Refs. 22, 23). Thick section joining on the order of 12 mm or greater of Alloy 690 will require higher laser powers than those available in the past. With increasing availability of higher power laser systems, deeper penetration welds are now possible. However, these deeper penetrations present other challenges and potential defects.

Porosity has been found to be a major obstacle for the implementation of laser welding Alloy 690 (Refs. 19–21). In general, there are three possible types of porosity that can form during welding. One type of porosity results from the high solubility of monatomic and diatomic O, N, and H in molten metal and

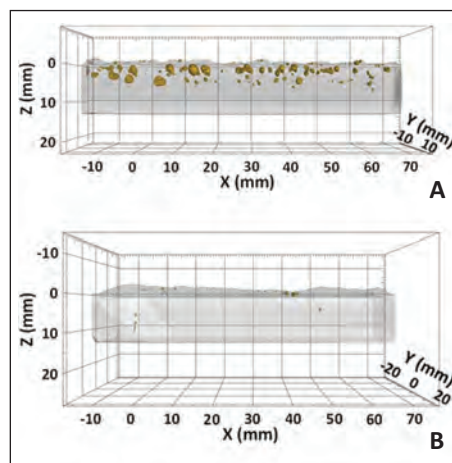


Fig. 3 — X-ray CT scans reveal the porosity in 6 kW 10 mm/s. A — Laser weld; B — hybrid weld. Hybrid welding significantly reduces the amount of porosity in the weld. The solid metal regions appear grey, while the pores are shown in a yellow color.

their corresponding low solubility in the solid metal (Ref. 24). During solidification, the solubility decreases, gas evolution occurs, and the bubbles become trapped as pores. Pore coalescence is another form of porosity in welds (Ref. 25) and is found in base metals with high pre-existing levels of porosity, such as die-cast magnesium alloys. For example, Zhao and DebRoy (Ref. 25) found an increase in porosity compared to the base metal during laser welding of die-cast Mg due to the expansion and coalescence of pre-existing pores during laser welding.

The third form of porosity is produced by keyhole instability, where the bottom tip of the keyhole fluctu-

Table 1 — Composition of the Alloy 690 Base Metal and Filler Metal 52

	Ni	Cr	Fe	Mn	Si	Ti	Al	Cu	C
Alloy 690	59.80	29.63	9.65	0.28	0.36	0	0	0.25	0.03
FM 52	60.88	29.22	8.65	0.24	0.14	0.38	0.4	0.01	0.02

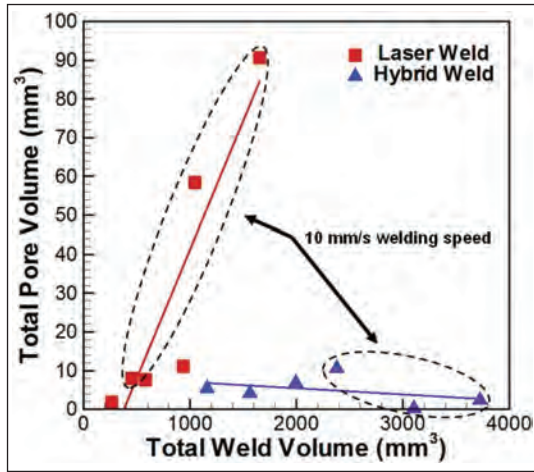


Fig. 4 — Total pore volume increases with the total weld volume in the laser welds, and the opposite relation is observed in the hybrid welds. Similarly, the low-speed laser welds had very high pore volume, while the same hybrid welds had relatively lower pore volume.

ates during welding and causes the vapor column to collapse, producing large bubbles, which can be trapped in the solidifying metal. Keyhole porosity is limited to high-energy beam welding processes (Ref. 18) and is by far the largest cause of macroporosity in laser and hybrid laser-arc welding (Refs. 26–29). Several researchers have investigated the effects of laser welding on keyhole porosity in Alloy 690. Kuo et al. (Ref. 9) found Alloy 690 to be more susceptible to the formation of keyhole porosity than AISI 304 stainless steel during pulsed laser welding. Tucker et al. (Ref. 10) found that porosity could only be minimized through the selection of laser defocus and welding speed but not entirely avoided.

Equilibrium vapor pressure-temperature relations (Refs. 30, 31), such as those shown in Fig. 1, may explain why Alloy 690 is more prone to keyhole porosity. An ideal solution is assumed for the calculation of vapor pressure, which is the sum of the product of the alloying element mole fraction and the vapor pressure for the

pure substance (i.e., Fe, Cr, Ni, Ti, Al, and V) at each temperature. Near the boiling point at 1 atmosphere, the temperature gradient of vapor pressure is higher for Alloy 690 as compared to other common structural alloys. As a result, small changes in temperature at the keyhole wall, which will be close to the boiling point, will produce larger changes in pressure, resulting in more instability and porosity.

Power modulation (Ref. 10), a defocused beam, and increased welding speeds have been shown to help to reduce porosity levels in laser welded Alloy 690, but there is no generally accepted methodology for eliminating keyhole porosity.

Experimental Methods

Bead-on-plate laser and hybrid laser-GMA welds were made on 12.7-

mm-thick Alloy 690 plate. For both the laser and hybrid welds examined here, the same combinations of laser welding conditions were used. A 200- μ m-diameter transport fiber connected an IPG Photonics® YLR-12000-L fiber laser to a YW50 Precitec® welding head. Within the head, the optics included a 200- and 500-mm focal length collimating and focusing lenses, respectively. A PRIMES® focus monitor beam characterization tool measured the beam diameter at focus and the divergence angle as 0.52 mm and 64 mrad, respectively.

The focus position was placed 8 mm below the top plate surface, so the beam diameter at the top surface was 0.73 mm. Consistent with beam characterization studies (Ref. 32), the beam profile near focus was top hat, while one Rayleigh length (8.1 mm in this case) or more from focus the beam

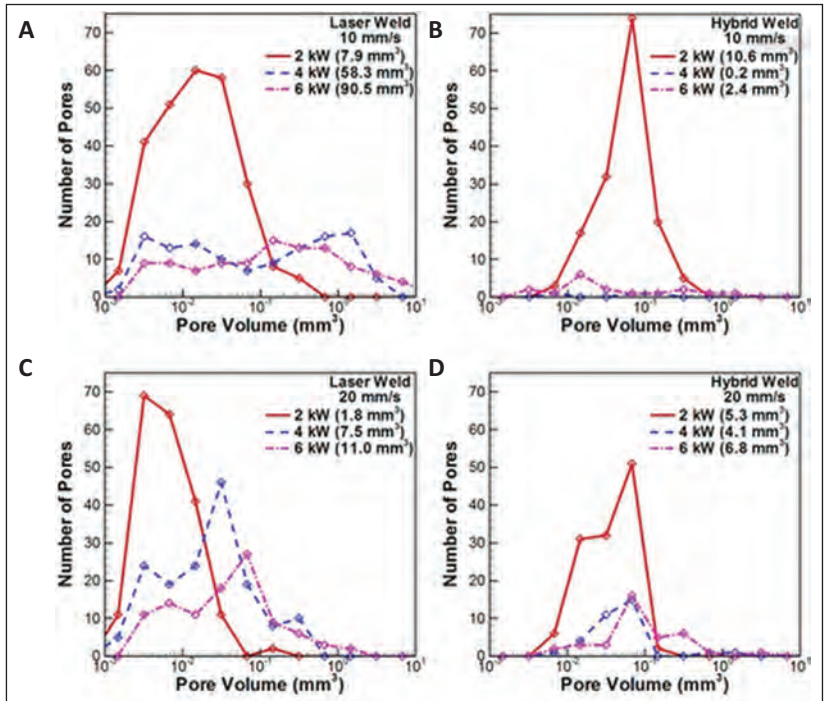


Fig. 5 — The porosity size distributions for (A and C) laser welds and (B and D) hybrid welds and the total porosity volumes in parentheses are shown. The number of pores for almost all sizes decrease when going from laser to hybrid welding at laser powers of 4 and 6 kW.

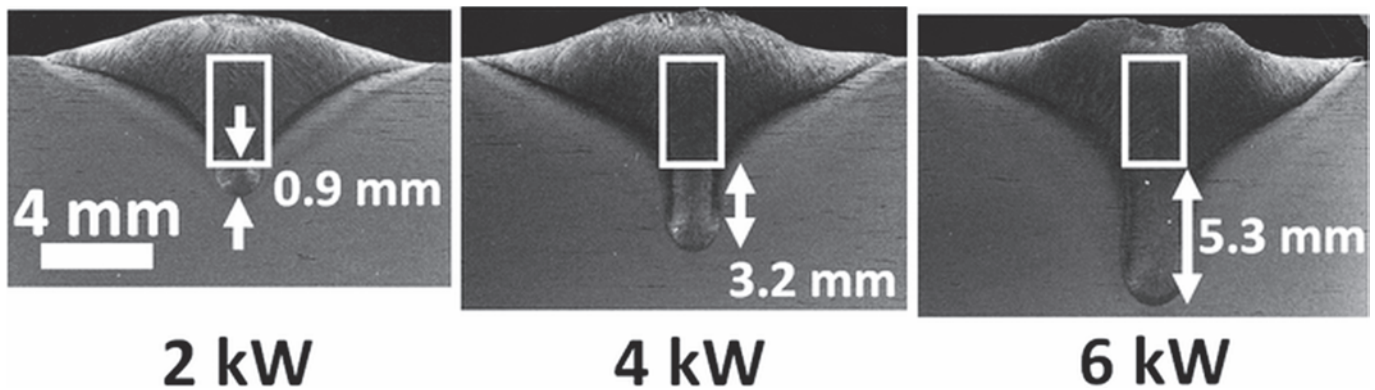


Fig. 6 — The calculated cylindrical volumetric heat source outline is overlaid on the 10 mm/s hybrid welds. The opening between the bottom of the heat source and weld bottom grows with laser power. The larger opening combined with a larger weld volume behind the opening led to more pores escaping in the 4- and 6-kW welds.

Table 2 — Summary of Weld Widths and Depths as a Function of Laser Power, Welding Speed, and Welding Technique

Power (kW)	Speed (mm/s)	Width (mm)		Depth (mm)	
		Laser	Hybrid	Laser	Hybrid
2	10	3.7	13.6	3.5	4.7
4	10	4.5	15.1	5.7	7.0
6	10	5.9	15.2	7.6	9.1
2	20	2.7	12.4	2.7	3.5
4	20	3.6	11.2	4.7	5.8
6	20	4.4	11.6	6.2	7.6

profile had a Gaussian shape. The welding speed and laser power were varied between 10 and 20 mm/s, and 2 and 6 kW, respectively.

For the hybrid welds, a Lincoln Electric® Power Wave 455 M/STT power source with a Binzel® WH 455D water-cooled welding gun were used. The torch angle was maintained at 15 deg from vertical. A gas mixture of Ar-25% He shielded the weld from the atmosphere at a 2.7 m³/h flow rate. Inconel® filler metal (FM) 52 wire with a diameter of 1.1 mm was used as the consumable electrode and is compositionally identical to Alloy 690, as shown in Table 1.

The wire feed speed was set to 121 mm/s. The laser-arc separation distance was held constant at 3 mm with the laser leading. The arc voltage was set to 32 V, and the current was estimated as 200 A based on the instantaneous values displayed on the power source, wire feed speed, and diameter of the filler metal wire. Standard metallographic techniques were used to prepare and analyze transverse cross-

section samples removed from locations in each weld where steady state processes are expected. The samples were electrolytically etched in a 10 wt-% oxalic acid solution.

A General Electric® v|tome|x x-ray CT system was used to inspect and characterize the internal porosity in each weld. X-ray CT provides a high degree of spatial resolution for the precise location and size of internal defects, such as pores (Ref. 33). An accelerating voltage of 250 kV and current of 200 μA were used to image the laser welds. Because the hybrid welds were approximately 10 mm wider at the top surface of the weld than the relatively narrow laser welds, the voltage and current were increased to 285 kV and 230 μA, respectively, during imaging of the hybrid welds. Using these combinations of accelerating voltage and current, the resolution in all directions was 50 and 66 μm for the laser and hybrid welds, respectively. DatosX® software reconstructed the individual x-ray images into a 3D representation. Vol-

ume Graphics® VGStudio Max software with the defect detection module was used to measure the sizes and locations of individual pores within the welds.

Results and Discussion

The fusion zone geometry is an important characteristic for comparing partial-penetration laser and hybrid welds. For example, the depth of the weld is related to the maximum weldable plate thickness in a single pass, and the width than is related to the plate opening bridgeability, which allows for higher tolerances during plate fitup before welding. Generally, hybrid welds have a greater width than and a similar depth to laser welds. Transverse weld profiles obtained from a series of laser and hybrid welds produced here are shown in Fig. 2.

The linear heat input during laser welding was varied between 100 and 600 W/mm. On the other hand, the heat input during hybrid laser-arc welding was higher with the addition of the arc and ranged between 400 and 1200 W/mm. Alloy 690 does not exhibit a distinct fusion zone similar to steels since the nickel-based alloy does not undergo a phase transformation below the melting point and is provided in the annealed state with relatively large grains. Some grain growth can be observed near the fusion zone boundary in Fig. 2, especially at high heat inputs.

The measured weld pool widths and depths are shown in Table 2. For the laser welds, the width and depth in-

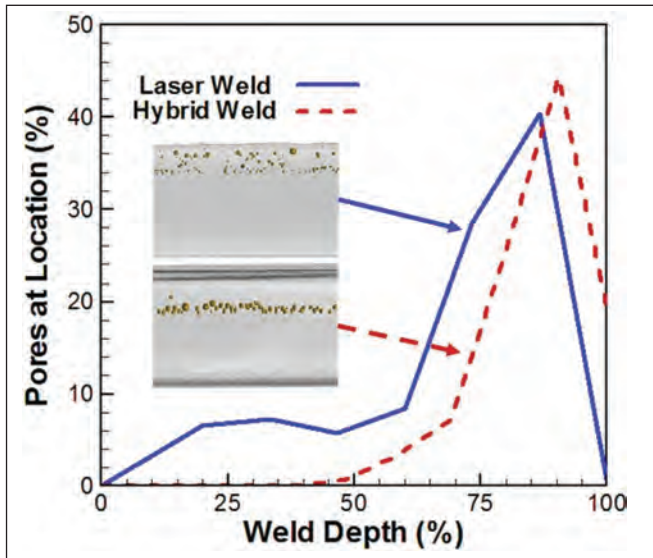


Fig. 7 — The pore location distributions in laser and hybrid welds for 2 kW of laser power and 10 mm/s welding speed are shown.

crease steadily with laser power, with a maximum width and depth of 5.9 and 7.6 mm, respectively, for a weld made at a laser power of 6 kW and a welding speed of 10 mm/s. Hybrid weld depth increases with power up to 9.1 mm at a laser power of 6 kW, but the width does not increase significantly and ranges from 11.2 to 15.2 mm across the power range from 2 to 6 kW. The hybrid weld widths are significantly greater than the laser weld widths due to the addition of the arc, which acts as a broad heat source. The difference between the laser and hybrid welds in width is 5 mm or more in most cases, while the depths of the hybrid welds are about 1 to 2 mm deeper than the laser welds under similar conditions.

Due to the addition of the arc and the increased heat input, the hybrid welds also display a much larger cross-sectional area than the laser welds. At laser powers of 2 kW, the influence of the arc on the hybrid weld pool shape is evident and dominates the characteristics of the weld pool. For example, the characteristic shape of a GMA weld (Ref. 34) is obvious at a welding speed of 20 mm/s, while at the very bottom of the weld, the finger penetration representative of a laser weld can be observed. Since the arc parameters are 31 V and about 200 A, the arc power is on the order of 6 kW, as compared to 2 kW for the laser. At higher laser powers of 4 and 6 kW, the influence of the

arc on the weld pool shape is diminished due to the parity in power of the arc and laser with only the increased width of the arc being evident.

Large pores in the solidified weld metal are formed when bubbles from the bottom of the keyhole become trapped by the advancing solid-liquid interface (Ref. 18). The keyhole tip near the bottom of the weld pool fluctuates rapidly and will pinch off regularly, creating bubbles in the liquid. While the role of the laser-induced keyhole in the formation of porosity in laser welding is understood, the effects of the addition of an arc in hybrid laser-arc are not. Using AISI 304 stainless steel as the base metal, Naito et al. (Ref. 35) found that keyhole-induced porosity is reduced but not entirely eliminated in hybrid laser-GTA welding compared to laser welding. This same relationship in Alloy 690 is explored here.

A comparison of porosity measured with x-ray CT in Alloy 690 laser and hybrid welds fabricated using the same laser power and welding speed (6 kW, 10 mm/s) is shown in Fig. 3. For the laser and hybrid laser-arc welds shown in Fig. 3, the level of porosity detected in the laser weld is much higher than that observed in the hybrid weld. For example, 103 pores were identified in

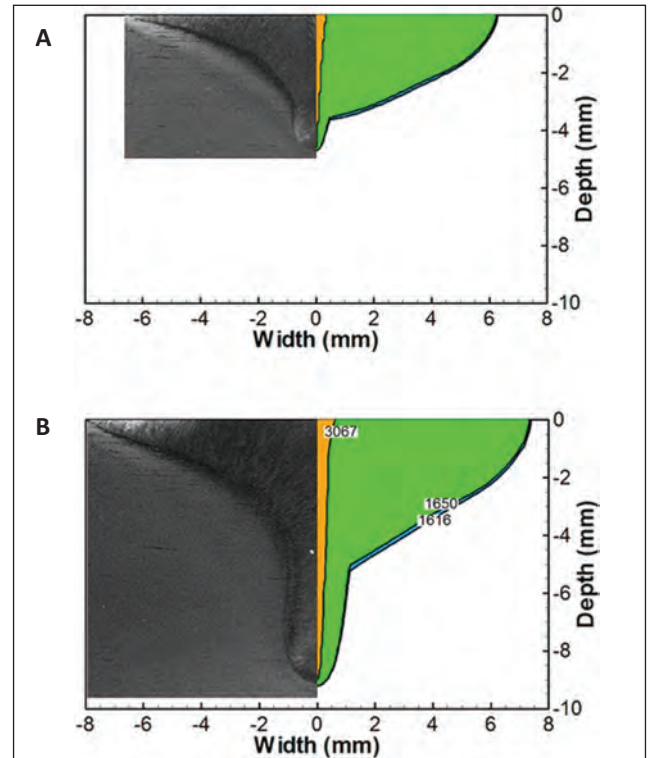


Fig. 8 — The experimental and calculated weld profiles for the hybrid welds made at 10 mm/s welding speed show reasonable agreement. A — 2 kW; B — 6 kW. The temperature contours are in Kelvin.

the x-ray CT scan with a median pore volume of 0.14 mm³, while only 17 pores were detected in the hybrid weld with a median pore volume of 0.02 mm³. In the hybrid welds, the locations of the detected pores is also important. For example, outside the start of the weld and the weld reinforcement, there is only one pore in the entire hybrid weld. This location on the weld can be separated from the weld region of interest by adding a 'run-on/run-off' tab that can be removed in a production environment.

The relationships between the total weld volume and the total pore volume over 70 mm of the laser and hybrid welds are shown in Fig. 4. In the laser welds, an increase in the total weld volume leads to an increase in pore volume. The hybrid welds, in general, exhibit a decrease in total pore volume as the welds become larger. In addition, the lower speed welds in each welding technique lead to different pore characteristics. The lowest pore volumes are found in the low-speed hybrid welds, while the highest pore volumes are found in the low-speed

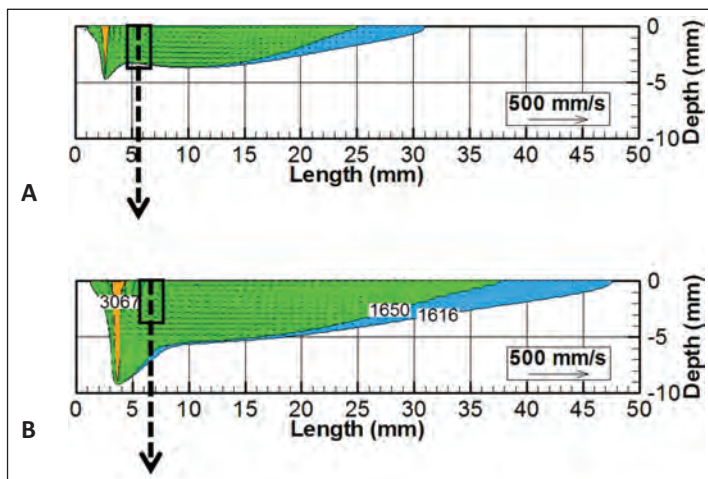


Fig. 9 — Calculated temperature and fluid velocity fields for the hybrid laser-arc welds with 10 mm/s welding speed. A — 2 kW; B — 6 kW. The outline of the volumetric heat source and the to-scale velocity vector of the impinging metal droplets is also shown.

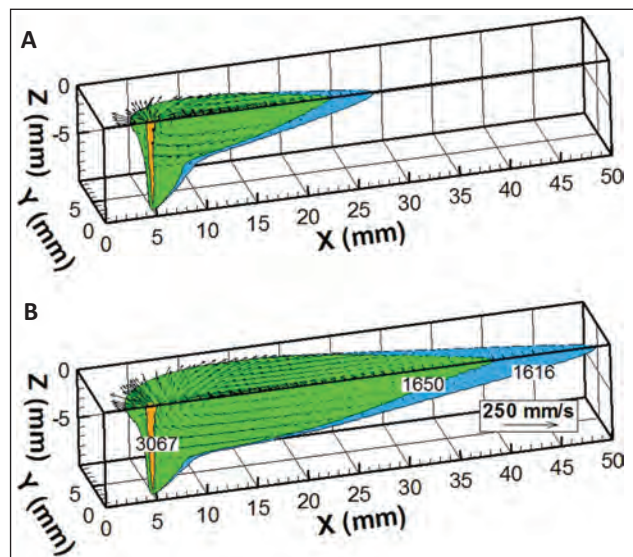


Fig. 10 — The 6 kW, 10 mm/s welds are shown for comparison. A — Laser; B — hybrid. In the larger hybrid weld, pores have a greater chance to escape the weld.

laser welds.

Total porosity volume and pore size distributions are important for understanding mechanisms driving porosity formation in laser and hybrid welds. Comparisons between the pore volume and pore size distributions in laser and hybrid welds produced under a variety of conditions are shown in Fig. 5. In the 4 and 6 kW cases, porosity decreased when transitioning from laser to hybrid welding. Clearly, the two highest heat input hybrid welds (4 and 6 kW and 10 mm/s) have the lowest porosity values. The 4-kW weld has only 3 pores with two of those located in the weld reinforcement. The laser welds with the same laser power and welding speed conditions show much higher overall porosity levels, which are up to 90.5 mm³ in 1600 mm³ of weld metal. These porosity levels are many times higher than the hybrid welds, which can have porosity values as low as 0.2 mm³ in 3000 mm³ of weld metal.

However, the trends of decreasing porosity in hybrid welds do not hold constant at lower powers. For example, the 2-kW, 10-mm/s hybrid weld does not show the same low porosity as the 4- and 6- kW hybrid welds and, in fact, has a higher porosity level than the laser weld made with the same conditions. The same is true in the welds made at this same power but a more rapid welding speed of 20 mm/s. This difference in behavior may be traced to a combination of filler metal

addition and small weld pool volume in the 2-kW hybrid welds. The filler metal is entering the molten pool at a relatively high rate of speed, on the order of 1.5 m/s or faster (Ref. 11).

Bubbles that form near the bottom of the keyhole need to move toward the top of the weld pool to escape. This mobility toward the top is likely hindered by the filler metal entering the pool at a high velocity. In addition, the pool volume is relatively small compared to the higher laser power welds, further limiting the bubble mobility toward the top of the pool. The laser welds exhibit a decrease in porosity with increasing speed and an increase in porosity with increasing laser power, which is consistent with previously reported experiments (Refs. 27, 36). For similar processing conditions, the differences in porosity between the laser and hybrid welds are related to the harmful or beneficial effects of the arc and impinging filler metal depending on the selected laser power.

The size of the filler metal-weld pool interaction region can be estimated using a cylindrical volumetric heat source (VHS) model (Ref. 12). A detailed description of the VHS model is available in the literature (Refs. 13, 14), and the equations necessary for the calculations performed here are available in Appendix A. The model assumes that liquid droplets are accelerated from the end of the consumable electrode, strike the molten pool, and

transfer heat and momentum to the weld. The height, depth, and energy intensity of the VHS can be calculated based on the material properties and welding parameters.

Knowledge of the relationship between the arc current and droplet detachment frequency is an important component of the calculations. Especially important is the transition current from globular to spray transfer. However, most studies of droplet detachment have focused on mild steel electrodes with little attention paid to other filler metals, such as FM 52. The welding recommendations for spray transfer mode from the FM 52 manufacturer have been used to estimate the transition currents (Ref. 37). The transition current for mild steel is around 290 A, so a current of 300 A or greater will lead to spray transfer mode. The recommended parameters for FM 52 suggest the transition current varies between 150 and 225 A, depending on the electrode diameter.

Using the experimental welding parameters and material properties, the VHS height and width can be computed. The height and width, which are identical for all hybrid welding cases, are calculated as 3.8 and 2.1 mm, respectively. The VHS profile has been overlaid on the transverse cross sections of the 10-mm/s welding speed hybrid welds in Fig. 6.

As the power increases, the opening

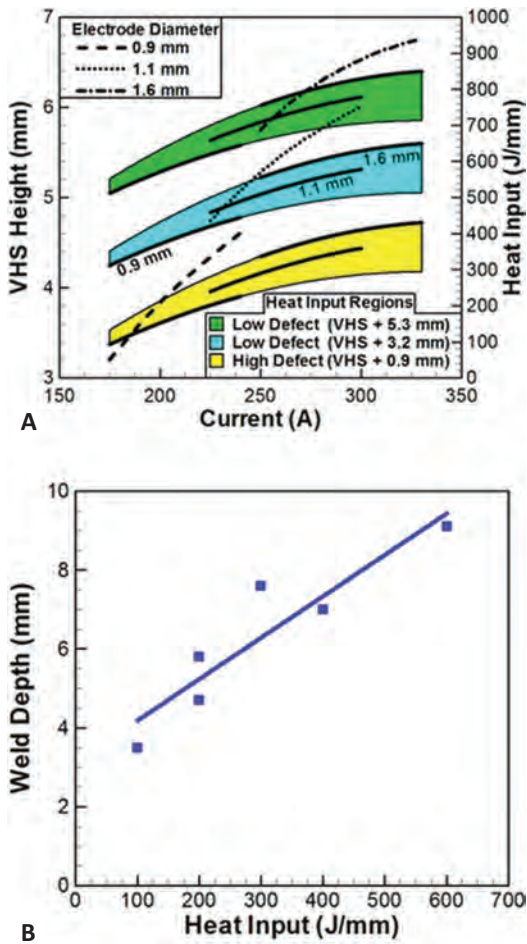


Fig. 11 — A — The volumetric heat source height for different arc currents and electrode diameters are shown. The laser heat inputs to provide different porosity values is also featured; B — the relation between weld depth and laser heat input used in A is shown.

between the bottom of the VHS and the bottom of the weld increases from 1 to more than 5 mm. The impinging droplet velocity, which is expected to interrupt pore motion through high fluid velocity turbulence, has a value of 1.6 m/s. The maximum calculated fluid flow velocity in a recent study of hybrid welding of steel was less than 0.3 m/s (Ref. 38), so the high velocity of the impinging droplets would have a significant impact on fluid flow in the weld pool and would interrupt the upward motion of pores escaping from the weld pool.

The evidence for this low mobility model can be extracted from Fig. 5, which shows a shift to higher pore sizes when going from laser to hybrid welding. This behavior is only seen in

the 2-kW welds and suggests that bubbles stay trapped at the bottom of the weld and combine to form larger bubbles before they are entrapped as pores by the advancing solidification front. In addition, the bubbles in the hybrid welds should be trapped in the bottom part of the weld and not show a great deal of variation in location distributions if the combination of the filler metal addition and small pool volume are limiting mobility.

Figure 7 shows the pore location distributions as a percentage of the total depth in the 2-kW, 10-mm/s laser and hybrid welds along with pertinent portions of the relevant x-ray CT images. In both welds, more pores are located near the bottom of the weld pool. In the laser weld, the top third of the weld contains 16% of the total number of the pores, but in the hybrid weld, zero pores are found in the same third of the weld.

Heat transfer and fluid flow modeling, which calculates the temperature and fluid velocity fields during welding, has been used successfully to simulate spot welding (Refs. 15, 39), arc welding (Ref. 12), and laser and hybrid laser arc welding for a variety of materials (Refs. 16, 17, 40, 41). The same model used recently to

simulate laser welding of Alloy 690 and hybrid laser-arc welding of steel has been utilized here to calculate the temperature and velocity fields during hybrid laser-GMA welding of Alloy 690 (Refs. 10, 38). The numerical model solves the equations of conservation of mass, momentum, and energy in 3D for enthalpy and fluid velocities. The keyhole heat source geometry is calculated using a point-by-point heat balance at the keyhole wall and then included into the 3D model. The addition of filler metal is taken into account as a volumetric heat source, while the arc is considered to have a Gaussian distribution on the surface. A comparison of the experimental and calculated fusion zone profiles for the hybrid welds made at 2- and 6-kW

laser power and 10-mm/s weld speed is shown in Fig. 8. The defocus in the 6 kW has been decreased to 2 mm to account for possible thermal lensing in the laser optics (Ref. 32). There is good agreement between the two values.

Figure 9 shows the central longitudinal plane of the 2- and 6-kW hybrid welds with 10-mm/s welding speed. The geometry of the VHS is outlined, and the large downward pointing arrow is the to-scale velocity vector of the impinging metal droplets from the consumable electrode. In the 2-kW weld, which had a high degree of porosity, the VHS height is approximately the depth of the pool 3 mm behind the laser beam. If a bubble forms near the bottom of the keyhole, it could easily be trapped in the advancing solid-liquid interface before it has a chance to escape. In the 6-kW weld, the minimum space between the bottom of the VHS and the pool below is 1.7 mm, which allowed for most bubbles to escape the pool and not be trapped in the solid as a pore. Laser welds had a much greater amount of porosity compared to the hybrid welds, especially at high laser powers and low welding speeds.

One reason for this difference in porosity content could be the relatively low volume of the laser welds as shown in Fig. 10, which shows the calculated temperature and fluid velocity fields in the 6-kW, 10-mm/s laser and hybrid welds. Due to the arc, the hybrid weld is not only wider but also longer by more than 20 mm. The low weld volume leading to high porosity in laser welds is similar to the low volume and filler metal addition leading to high porosity in the low laser power hybrid welds.

Since the likelihood of low porosity in the hybrid welds can be related to the distance between the bottom of the VHS and bottom of the weld, the weld depth and VHS height are two dimensions, which can be related to porosity. Arc current, FM 52 electrode diameter, and linear laser heat input are easily selectable welding parameters affecting these two important dimensions.

Figure 11 shows the combined effect of different combinations of the welding parameters in the form of a process map with wire feed speed in-

creased linearly with current for calculation purposes. The three nonsolid lines represent the effect of the current and electrode diameter on VHS height on the left y-axis. The three regions predict linear laser heat inputs for all electrode diameters that will lead to openings between the bottom of the VHS and the weld pool, corresponding to the openings observed in the experimental welds shown in Fig. 6 (0.9, 3.2, and 5.3 mm).

Heat inputs in the lower region result in openings of 0.9 mm, which was experimentally shown to have a high degree of porosity. VHS height-weld depth openings of 3.2 and 5.3 mm in the middle and top heat input regions, respectively, are expected to have a low degree of porosity. The solid lines in each heat input region designate the exact electrode diameter dependent heat inputs. The weld depth-heat input relationship from the experimental welds is shown in Fig. 11B.

The process map in Fig. 11A covers the range of electrode diameters and arc currents suggested for FM 52 (Ref. 37). For a given arc current and electrode diameter, a linear laser heat input is suggested to avoid porosity. For example, if a 1.6-mm electrode diameter and arc current of 300 A is selected, then the VHS height is predicted to be 6.5 mm. According to the top two regions, a laser heat input between 630 and 830 J/mm would produce a weld depth between 9.7 and 11.8 mm, and weld depth-VHS height differences between 3.2 and 5.3 mm, which have been shown experimentally to lead to low porosity. On the other hand, a heat input of 410 J/mm yields a weld depth of 7.4 mm with only a 0.9 mm difference between the VHS height and weld depth. Based on experiments, this small difference is expected to lead to a high porosity content.

As shown in Fig. 8, VHS height increases with both current and electrode diameter. According to the graph, the minimum heat input from the laser for low porosity increases with both arc current and electrode diameter. The minimum heat input for the 1.1-mm-diameter filler metal is 460 J/mm. For the 0.9- and 1.6-mm-diameter electrodes, the minimum heat inputs are 310 and 550 J/mm, respectively. For a 10-mm/s welding

speed, reasonable laser powers of 5 to 6 kW can be used to fabricate low porosity welds up to 9.0 mm in depth with any FM 52 electrode diameter. However, if greater productivity is desired in terms of welding speed or penetration depth, much higher powers will be required. For example, an increase of the welding speed to 20 mm/s would require 11-kW laser power to make pore-free welds with 1.6-mm-diameter electrodes.

Summary and Conclusions

The characteristics of laser and hybrid laser-gas metal arc welded Alloy 690 with a compositionally identical filler metal have been analyzed for several welding conditions experimentally and theoretically. Experimental characterization of total porosity amounts was performed with x-ray CT. Transverse fusion zone geometries and porosity resulting from keyhole collapse for both laser and hybrid welds have been compared and found to have significant differences, thus affecting the choice of a suitable welding process. The following conclusions were drawn from this work.

1. An analysis of Alloy 690 vapor pressure at various temperatures shows that the equilibrium vapor pressures are very sensitive to small changes in temperature, making Alloy 690 susceptible to macroporosity due to keyhole fluctuations during high-power laser welding. X-ray CT data revealed significant levels of macroporosity in keyhole-mode laser welds for a wide variety of welding conditions.

2. The addition of an arc to a laser beam significantly reduced porosity levels in the high-power welds. The lowest levels of porosity were observed in the hybrid welds at powers of 4 and 6 kW and a welding speed of 10 mm/s. A minimum porosity total of 0.2 mm³ in a total weld volume of 3000 mm³ was found in a hybrid weld with 4-kW laser power and 10-mm/s welding speed. In contrast, a laser weld made at a power of 6 kW and a travel speed of 10 mm/s displayed a porosity volume of 90.5 mm³ in 1600 mm³ of weld metal.

3. A transition from high levels of porosity to virtually no porosity was observed in the hybrid welds as power increased above 2 kW. The combination of the experimental weld charac-

terization, calculations of the filler metal-molten pool mixing region dimensions, and three-dimensional heat transfer and fluid flow modeling suggests that the mechanism of this high porosity is linked to the relative sizes of the molten pool and filler metal-molten pool mixing region. Filler metal transfer and low weld pool volume at 2-kW laser power limit upward bubble mobility out of the pool by impeding bubble motion and restricting the regions in which the bubbles can move. As the power increases, the size of the filler metal mixing region relative to the weld pool decreases, allowing the bubbles to more easily escape.

4. Experimental evidence of this mechanism included a shift in the pore size distribution to larger pores when going from laser to hybrid welding and more pores located at the bottom of the pool in hybrid welding compared to laser welding. In addition, three-dimensional heat transfer and fluid flow modeling showed no opening between the bottom of the filler metal-molten pool mixing region and the bottom of the weld pool, while at higher powers, this opening increases to 2 mm and allows easy escape of the bubbles during welding. The 2-mm-wide opening is larger than most, approximately 97% of the observed pore diameters.

5. The remedy for high porosity lies in a minimum opening between the weld depth and filler metal-weld pool mixing region. Calculations accounting for the volumetric heat source dimensions, weld depths, and FM 52 electrode dimensions were incorporated into a process map to establish the combinations of arc current, linear laser heat input, and filler metal wire diameter needed to produce low-porosity hybrid laser-arc welds. The minimum heat input varied between 240 and 490 J/mm with greater heat inputs required for larger electrode diameters. With welding speeds of 10 mm/s or less, no more than 5-kW laser power would be required to produce pore-free welds with every electrode diameter. Increasing welding speed or current to improve productivity or filler metal deposition would require higher laser powers.

Based on the results of this study, hybrid welding is recommended for welding thick sections of Alloy 690, especially at laser powers above 2 kW.

The large amounts of porosity in the laser welds are mostly eliminated when the arc is appropriately added to the process using the proposed process map. With optimized process parameters, macroporosity-free thick section welds could be produced by hybrid welding.

Acknowledgments

The authors would like to thank Jay Tressler for performing the welding experiments and Ed Good for preparing the metallographic and x-ray specimens. This research was performed using funding received from the DOE Office of Nuclear Energy's Nuclear Energy University Programs under Grant Number 120327.

References

- Allen, T., Busby, J., Meyer, M., and Petti, D. 2010. Materials challenges for nuclear systems. *Mater. Today* 13(12): 14–23.
- Lee, H. T., and Kuo, T. Y. 1999. Effects of niobium on microstructure, mechanical properties, and corrosion behavior in weldments of Alloy 690. *Sci. Technol. Weld. Join.* 4(4): 245–256.
- Jeng, S.-L., Lee, H.-T., Huang, J.-Y., and Kuo, R.-C. 2008. Effects of Nb on the microstructure and elevated-temperature mechanical properties of Alloy 690-SUS 304L dissimilar welds. *Mater. Trans.* 49(6): 1270–1277.
- Lee, H. T., and Kuo, T. Y. 1999. Analysis of microstructure and mechanical properties in Alloy 690 weldments using filler metals I-82 and I-52. *Sci. Technol. Weld. Join.* 4(2): 94–103.
- Lee, H. T., and Jeng, S. L. 2001. Characteristics of dissimilar welding of Alloy 690 to 304L stainless steel. *Sci. Technol. Weld. Join.* 6(4): 225–234.
- Jeng, S. L., Lee, H. T., Weirich, T. E., and Rebach, W. P. 2007. Microstructural study of the dissimilar joints of Alloy 690 and SUS 304L stainless steel. *Mater. Trans.* 48(3): 481–489.
- Ribic, B., Palmer, T. A., and DebRoy, T. 2009. Problems and issues in laser-arc hybrid welding. *Int. Mater. Rev.* 54(4): 223–244.
- Kuo, T.-Y. 2005. Effects of pulsed and continuous Nd-YAG laser beam waves on welding of Inconel alloy. *Sci. Technol. Weld. Join.* 10(5): 557–565.
- Kuo, T.-Y., and Lin, Y.-D. 2007. Effects of different shielding gases and power waveforms on penetration characteristics and porosity formation in laser welding of Inconel 690 Alloy. *Mater. Trans.* 48(2): 219–226.
- Tucker, J. D., Nolan, T. K., Martin, A. J., and Young, G. A. 2012. Effect of travel speed and beam focus on porosity in Alloy 690 laser welds. *JOM* 64(12): 1409–1417.
- Jones, L. A., Eagar, T. W., and Lang, J. H. 1999. A dynamic model of drops detaching from a gas metal arc welding electrode. *J. Phys. D. Appl. Phys.* 31(1): 107–123.
- Kim, C. H., Zhang, W., and DebRoy, T. 2003. Modeling of temperature field and solidified surface profile during gas-metal arc fillet welding. *J. Appl. Phys.* 94(4): 2667–2679.
- Lancaster, J. F. 1986. *The Physics of Welding*. 2nd ed. Oxford: Pergamon.
- Kumar, S., and Bhaduri, S. 1994. Three-dimensional finite element modeling of gas metal-arc welding. *Metall. Mater. Trans. B* 25(3): 435–441.
- Zhang, W., Roy, G. G., Elmer, J. W., and DebRoy, T. 2003. Modeling of heat transfer and fluid flow during gas tungsten arc spot welding of low carbon steel. *J. Appl. Phys.* 93(5): 3022–3033.
- Rai, R., Elmer, J. W., Palmer, T. A., and DebRoy, T. 2007. Heat transfer and fluid flow during keyhole mode laser welding of tantalum, Ti-6Al-4V, 304L stainless steel and vanadium. *J. Phys. D. Appl. Phys.* 40(18): 5753–5766.
- Ribic, B., Rai, R., and DebRoy, T. 2008. Numerical simulation of heat transfer and fluid flow in GTA/Laser hybrid welding. *Sci. Technol. Weld. Join.* 13(8): 683–693.
- Matsunawa, A., Kim, J.-D., Seto, N., Mizutani, M., and Katayama, S. 1998. Dynamics of keyhole and molten pool in laser welding. *J. Laser Appl.* 10(6): 247–254.
- Blecher, J. J., Galbraith, C. M., Van Vlack, C., Palmer, T. A., Fraser, J. M., Webster, P. J. L., and DebRoy, T. 2014. Real time monitoring of laser beam welding keyhole depth by laser interferometry. *Sci. Technol. Weld. Join.* 19(7): 560–564.
- Lee, H. T., Chen, C. T., and Wu, J. L. 2010. 3D numerical study of effects of temperature field on sensitisation of Alloy 690 butt welds fabricated by gas tungsten arc welding and laser beam welding. *Sci. Technol. Weld. Join.* 15(7): 605–612.
- Blecher, J. J., Palmer, T. A., and DebRoy, T. 2013. Solidification map of a nickel-base alloy. *Metall. Mater. Trans. A* 45(4): 2142–2151.
- Suder, W. J., and Williams, S. 2014. Power factor model for selection of welding parameters in CW laser welding. *Opt. Laser Technol.* 56: 223–229.
- Quintino, L., Costa, A., Miranda, R., Yapp, D., Kumar, V., and Kong, C. J. 2007. Welding with high power fiber lasers – A preliminary study. *Mater. Des.* 28(4): 1231–1237.
- Kou, S. 2003. *Welding Metallurgy*. 2nd ed. Hoboken, N.J.: John Wiley & Sons, Inc.
- Zhao, H., and DebRoy, T. 2001. Pore formation during laser beam welding of die-cast magnesium alloy AM60B — Mechanism and remedy. *Welding Journal* 80(8): 204-s to 210-s.
- Katayama, S., Kobayashi, Y., Mizutani, M., and Matsunawa, A. 2001. Effect of vacuum on penetration and defects in laser welding. *J. Laser Appl.* 13(5): 187–192.
- Kawahito, Y., Mizutani, M., and Katayama, S. 2007. Elucidation of high-power fibre laser welding phenomena of stainless steel and effect of factors on weld geometry. *J. Phys. D. Appl. Phys.* 40(19): 5854–5859.
- Zhao, H., Martukanitz, R. P., and DebRoy, T. 1999. Porosity, underfill and magnesium loss during continuous wave Nd: YAG laser welding of thin plates of aluminum Alloys 5182 and 5754. *Welding Journal* 78(6): 207-s to 216-s.
- Zhao, H., and DebRoy, T. 2003. Macroporosity free aluminum alloy weldments through numerical simulation of keyhole mode laser welding. *J. Appl. Phys.* 93(12): 10089–10096.
- Smithells, C. 2004. *Smithells Metals Reference Book*. 8th ed. Boston: Elsevier Butterworth-Heinemann.
- Yaws, C. L. 2007. *The Yaws Handbook of Vapor Pressure: Antoine Coefficients*. Houston: Gulf Publishing Co.
- Blecher, J., Palmer, T. A., Kelly, S. M., and Martukanitz, R. P. 2012. Identifying performance differences in transmissive and reflective laser optics using beam diagnostic tools. *Welding Journal* 91(7): 204-s to 214-s.
- Madison, J. D., and Aagesen, L. K. 2012. Quantitative characterization of porosity in laser welds of stainless steel. *Scr. Mater.* 67(9): 783–786.
- Yang, Z., and DebRoy, T. 1999. Modeling macro- and microstructures of gas-metal-arc welded HSLA-100 steel. *Metall. Mater. Trans. B-Process Metall. Mater. Process. Sci.* 30(3): 483–493.
- Naito, Y., Katayama, S., and Matsunawa, A. 2003. Keyhole behavior and liquid flow in molten pool during laser-arc hybrid welding. *Proc. SPIE* 4831: 357–362.
- Kawahito, Y., Mizutani, M., and Katayama, S. 2009. High quality welding of stainless steel with 10 kW high power fibre laser. *Sci. Technol. Weld. Joining* 14(4): 288–294.
- Special Metals Corp., “Joining,” accessed 30 April 2015, pg. 9, specialmetalswelding.com.
- Wei, H. L., Blecher, J. J., Palmer, T.

A., and DebRoy, T. 2015. Fusion zone microstructure and geometry in complete-joint-penetration laser-arc hybrid welding of low-alloy steel. *Welding Journal* 94(4): 135-s to 144-s.

39. He, X., Fuerschbach, P. W., and DebRoy, T. 2003. Heat transfer and fluid flow during laser spot welding of 304 stainless steel. *J. Phys. D. Appl. Phys.* 36(12): 1388–1398.

40. Rai, R., Roy, G. G., and Debroy, T. 2007. A computationally efficient model of convective heat transfer and solidification characteristics during keyhole mode laser welding. *J. Appl. Phys.* 101(5): 054909.

41. Rai, R., Kelly, S. M., Martukanitz, R. P., and DebRoy, T. 2008. A convective heat-transfer model for partial and full penetration keyhole mode laser welding of a structural steel. *Metall. Mater. Trans. A Phys. Metall. Mater. Sci.* 39(1): 98–112.

42. Rhee, S., and Kannatey-Asibu, E. 1992. Observation of metal transfer during gas metal arc welding. *Welding Journal* 71(10): 381-s to 386-s.

43. Kim, G.-H., and Na, S.-J. 2001. A study of an arc sensor model for gas metal arc welding with rotating arc Part 1: dynamic simulation of wire melting. *Proc. Inst. Mech. Eng. Part B J. Eng. Manuf.* 215(9): 1271–1279.

44. Waszink, J. H., and Van Den Heuvel, G. J. P. M. 1982. Heat generation and heat flow in the filler in GMA welding. *Welding Journal* 61(8): 269-s to 280-s.

Appendix A

Calculation of Volumetric Heat Source Dimensions

The volumetric heat source (VHS) calculation assumes a cylindrical shape with dimensions of diameter and height. The VHS is commonly used to model consumable electrode heat transfer during gas metal arc welding (Refs. 12, 14). In these experiments, spray metal transfer, where small droplets form at the end of the electrode and accelerate into the molten pool, is expected. Several variables are required for the calculation, including material properties, welding parameters, and droplet frequency.

The height of the VHS is given as $d = h_v - x_v + D_d$, where h_v is height of the cavity formed by the impinging droplets, x_v is the distance traveled in the cavity by each droplet before the arrival of the next impinging droplet,

and D_d is the droplet diameter. The cavity height is

$$h_v = \left(-\frac{2\gamma}{D_d\rho g} + \sqrt{\left[\left(\frac{2\gamma}{D_d\rho g} \right)^2 + \frac{D_d v_d^2}{6g} \right]} \right) \quad \text{A1}$$

where γ is surface tension of the liquid metal, ρ is the liquid metal density, g is acceleration due to gravity, and v_d is the droplet impingement velocity. The surface tension and density of FM 52 were taken as 1.1 N/m and 6500 kg/m³, respectively. The distance traveled by each droplet is defined as

$$x_v = \left(h_v + \frac{2\gamma}{D_d\rho g} \right) \left\{ 1 - \cos \left[\left(\frac{g}{h_v} \right)^{1/2} \Delta t \right] \right\} \quad \text{A2}$$

where Δt is the time interval between the impingement of two droplets and can be defined as $\Delta t = 1/f$. The frequency of droplets, f , is

$$f = \frac{-243.44}{1 + \exp\left(\frac{I - I_t}{6.06437}\right)} + 323.506 - 0.874I + 0.0025I^2 \quad \text{A3}$$

where I (A) is the current and I_t is the transition current from globular to spray transfer. The transition current for FM 52 has been estimated based on the suggested process parameters by the electrode manufacturer (Ref. 37).

The frequency current relations are shown in Fig. A1 for three FM 52 electrode diameters and, for reference (Refs. 11, 42), a fitted line to experimental data for mild steel. The droplet shape is assumed to be spherical, and the radius of the sphere is expressed as

$$r_d = \sqrt[3]{\frac{3}{4} r_w^2 w_f / f} \quad \text{A4}$$

where r_w is the radius of the filler metal wire and w_f is the wire feed speed. The VHS diameter is four times the droplet radius. The droplet velocity is

$$v_d = \sqrt{v_0^2 + 2aL_a} \quad \text{A5}$$

where v_0 is the initial velocity, a is the droplet acceleration, and L_a is the arc length. The calculation for the arc

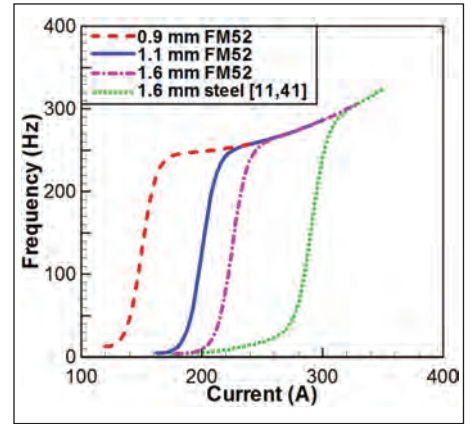


Fig. A1 — The current-droplet detachment frequencies for FM 52 are not experimentally known. Based on suggested currents, voltages, shielding gases, and wire feed speeds for different electrode diameters from the manufacturer, the relations have been estimated. The fit line for experimental data for steel in Ar-5%CO₂ shielding gas is shown for reference.

length (Ref. 43) and measured electrode extension length (Ref. 44) are available in the literature. Acceleration is taken as

$$a = \frac{3 v_g^3 \rho_g}{8 r_d \rho} C_d + g \quad \text{A6}$$

where v_g is the velocity of the plasma, ρ_g is the density of the plasma, and C_d is the drag coefficient. The plasma density was taken as 0.06 kg/m³. The velocity of the plasma is estimated with the effective velocity (in m/s), which is $v_{eff} = k_1 \times I$, where k_1 is a constant coefficient of ¼. The drag coefficient is $C_d = -242.74Re^{-2} + 59.67Re^{-1} + 0.44793$, where Re is the Reynolds number, which is defined as $Re = r_d v_{eff} / \nu_k$. The variable ν_k is kinetic viscosity and is 3.4×10^{-3} m²/s. The initial velocity is calculated as

$$v_0 = \sqrt{-0.33692 + 0.00854 (I/D_d)} \quad \text{A7}$$